Confocal acoustic radiation force optical coherence elastography using a ring ultrasonic transducer

Wenjuan Qi, Rui Li, Teng Ma, K. Kirk Shung, Qifa Zhou, and Zhongping Chen

Citation: Applied Physics Letters **104**, 123702 (2014); doi: 10.1063/1.4869562
View online: http://dx.doi.org/10.1063/1.4869562
View Table of Contents: http://scitation.aip.org/content/aip/journal/apl/104/12?ver=pdfcov
Published by the AIP Publishing

Confocal acoustic radiation force optical coherence elastography using a ring ultrasonic transducer

Wenjuan Qi,[1,2,a)] Rui Li,[1,a)] Teng Ma,[3,a)] K. Kirk Shung,[3] Qifa Zhou,[3] and Zhongping Chen[1,2,4,b)]

[1]*Beckman Laser Institute, University of California, Irvine, 1002 Health Sciences Road East, Irvine, California 92612, USA*
[2]*Department of Chemical Engineering and Materials Science, University of California, Irvine, Irvine, California 92697, USA*
[3]*Department of Biomedical Engineering, NIH Ultrasonic Transducer Resource Center, University of Southern California, Los Angeles, California 90089, USA*
[4]*Department of Biomedical Engineering, University of California, Irvine, Irvine, California 92697, USA*

(Received 30 October 2013; accepted 13 March 2014; published online 27 March 2014)

We designed and developed a confocal acoustic radiation force optical coherence elastography system. A ring ultrasound transducer was used to achieve reflection mode excitation and generate an oscillating acoustic radiation force in order to generate displacements within the tissue, which were detected using the phase-resolved optical coherence elastography method. Both phantom and human tissue tests indicate that this system is able to sense the stiffness difference of samples and quantitatively map the elastic property of materials. Our confocal setup promises a great potential for point by point elastic imaging *in vivo* and differentiation of diseased tissues from normal tissue.
 [http://dx.doi.org/10.1063/1.4869562]

The mechanical properties of living tissue are critical indicators of tissue pathological conditions as many diseases progress with mechanical alterations. Particularly in the diagnosis of atherosclerosis, the major cause of cardiovascular death in heart attacks (86%), knowledge of vessel mechanical properties can be used to analyze plaque vulnerability.[1] To measure the mechanical property information, physicians have used manual palpation for centuries to roughly estimate the mechanical properties of the internal organs. However, the accuracy of this method is limited by the size and location of the pathological lesion.

Elastography is an emerging imaging technique that assesses mechanical properties of tissue by measuring the local deformation of tissue induced by external or internal stimulation.[2] Elastography has been applied to a range of imaging modalities. Magnetic resonance elastography (MRE), ultrasound (US) elastography, and optical coherence elastography (OCE) are three main elastographic imaging techniques currently being investigated.

MRE is a phase-contrast-based Magnetic Resonance Imaging (MRI) technique. By directly visualizing and quantitatively measuring propagating acoustic strain shear waves induced by harmonic mechanical excitation, MRE is capable of quantitatively predicting the shear modulus of the subject. Ultrasound is another elasticity imaging technique intensively used.[3–5] Using either speckle tracking or the Doppler velocity method, this technique demonstrates great potential for assessing tissue stiffness. Since first being introduced, both of the methods have been currently applied to the diagnosis of cancers, intravascular diseases, and fibrosis.[3–8] However, the resolution, usually from a few hundred micrometers to several millimeters, of these techniques limits their clinical applications, especially, for detection of small atherosclerotic lesions and plaque composition analysis in small arteries.

OCE is an emerging elasticity imaging technique being investigated and developing rapidly in recent years.[9–16] Based on traditional optical coherence tomography (OCT) technique, OCE overcomes the resolution limitation of MRE and US elastography techniques by detecting nano-to-micron-scale internal local deformation of the subject. OCE is used to measure shear wave,[15] longitudinal vibration,[16] and surface acoustic wave propagation,[17] which are further used to quantify shear modulus or Young's modulus. The OCE technique has been used to investigate the biomechanical properties of both engineered tissue and living tissue such as skin, muscle, cornea, and blood vessel.[13,14,16,18,19] However, most of the current OCE techniques detect the shear wave propagation which greatly limit their imaging speed. There are OCE methods that use dynamic excitation to achieve high speed; however, the mechanical loading method limits accessibility to internal organs such as arteries and retina. Therefore, there are still significant challenges to apply OCE technique for *in vivo* intravascular imaging and ophthalmic imaging.

We have previously developed a phase-resolved acoustic radiation force optical coherence elastography (ARF-OCE) system with the capability of transient elastographic imaging of tissue mechanical property.[16] Our method combines high-speed dynamic acoustic radiation force excitation and high sensitivity phase-resolved OCT detection to measure local tissue displacement in an axial direction, which provides a means of localized point-by-point quantification of tissue response to ARF palpation and representation of tissue stiffness. In contrast to OCE based on shear wave propagation that can only apply to relatively flat tissue,[15,17] our phase-resolved ARF-OCE can be applied to any tissue geometry. However, the previous reported system used a transmission mode where the ultrasound transducer and optical detection were located on opposite sides of the tissue. In order to have compatibility

[a)]W. Qi, R. Li, and T. Ma contributed equally to this work.
[b)]Author to whom correspondence should be addressed. Electronic mail: z2chen@uci.edu.

with a catheter design for intravascular imaging, in this paper, we have further improved the system by using a ring transducer to achieve co-registered excitation and detection from the same tissue side. The benefit from this confocal configuration is that the adaptation for an endoscopic probe can be achieved by using the confocal configuration. Moreover, because of the high sensitivity of phase-resolved OCT, only minimal force needs to be applied to the object in order to generate the elastogram, which is most desirable for non-invasive intravascular imaging. Finally, the proposed system configuration provides more accurate local displacement information and holds promise for *in vivo* endoscopic intravascular elastography for imaging and quantifying atherosclerosis as well as ophthalmic elastography for imaging and quantifying drusen deposition in age related macular degeneration disease.

The schematic of the confocal ARF-OCE system is shown in Fig. 1(a). The system is based on an 890 nm spectral domain OCT (SD-OCT) system. The acquisition rate of this system was 20 kHz. The axial and lateral resolutions of the system were measured to be 3.5 and 14.8 μm, respectively. The signal-to-noise-ratio (SNR) of the system was 100 dB with 650 μW of sample arm power and a 50-μs A-line rate. The minimum detectable phase for this system was measured to be 1.5 mrad, which corresponded to a velocity sensitivity of 2.13 μm/s and a displacement sensitivity of less than 1 nm. A water cell was inserted in the reference arm in the SD-OCT system to compensate for the dispersion induced by the water in the sample arm.

Unlike our previously published experimental setup with a transmission mode where the US transducer excites the sample from the bottom and optical detection is from the opposite direction, this experimental design features a reflection mode. In this configuration, the acoustic excitation and OCT detection are arranged in a way so that the light and the ultrasound shine on the sample from the same side and completely overlap with each other at the focal point where the sample will be placed. A custom-made focused-ring ultrasound transducer [Fig. 1(b)] with a 5 mm hole at the center to make room for the OCT probing beam was used to achieve the reflection confocal mode. To generate enough acoustic radiation force at 50 mm focal depth and coordinate with the optical scanning setup, the center frequency of ultrasonic transducer was designed to be 4 MHz and stable piezoelectric ceramic lead zirconium titanate (PZT) was selected as the functional material. The acoustic induced vibrational area was directly related to the beam diameter of the ultrasonic transducer defined in the following equation:

$$BD = 1.02\left(\frac{c}{f}\right)F\#, \tag{1}$$

where BD is the beam diameter (−6 dB), c is the speed of sound, f is the center frequency, and F# is the ratio of the focal depth and diameter of the ultrasonic transducer. Similarly to the articles reported by Sun *et al.*,[20,21] the acoustic output and sensitivity of the ring transducer would be reduced compared to a standard focused transducer due to loss of inner functional material. However, according to the Field II simulation in Fig. 1(c), the acoustic beam characteristics of the ring transducer at the focal zone did not have significant change. Therefore, the ring transducer could still provide similar OCT-detectable displacements in the focal zone as a standard focused transducer. Because the focal length of the US transducer is 50 mm, an objective lens with a 70 mm focal length in the OCT detection arm was used so that the focal point of the US transducer and the OCT probing light could overlap with each other.

To generate the acoustic radiation force, the transducer was placed about 20 mm below the objective lens of the OCT system so that the focus of both the light and ultrasound beam overlap. For all the experimental imaging, the samples were positioned in such a plane that a relatively large area of uniform ARF could be obtained for displacement measurement. An experiment from a homogeneous phantom confirmed that the ARF induced displacement was uniform over a 1.5 mm lateral length, as shown in Figure 2. Since the light beam width is about 14.8 μm, which is much less than the ultrasound beam width and the acoustic field is evenly distributed, it allows the light to scan within a 1.5 mm length. For all the experiments, the scanning area was confined within a 0.5 mm × 0.3 mm area where we assumed that the acoustic field was uniform. The transducer was driven by a signal that was amplitude modulated by a square wave to generate a periodic acoustic radiation force perpendicularly onto the sample. The pulse delay generator (DS345, Stanford Research Systems, USA) generated a low kHz square wave (50% duty cycle amplitude modulation-AM) which modulated the amplitude of the 4 MHz burst generated by the function generator (33220A, Agilent Technologies, USA). Then the modulated signal was amplified by a RF power

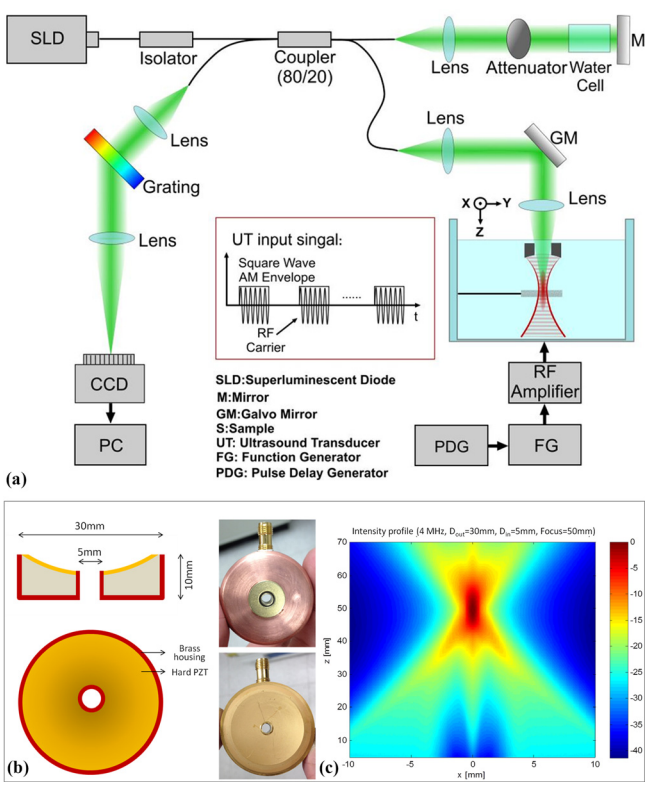

FIG. 1. (a) Schematic of the confocal ARF–OCE system, including a SD-OCT system and a customized focused ring transducer (4 MHz). (b) Photograph and (c) Field II simulation for the intensity profile of the customized focused ring transducer with a 30 mm aperture and a 5 mm hole in the center.

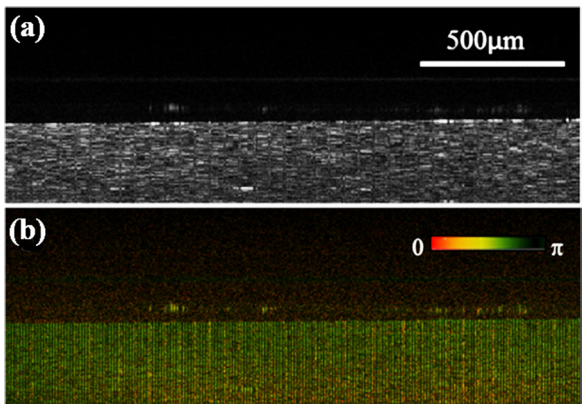

FIG. 2. Scanning area validation on a homogeneous silicone phantom with 1.5 mm lateral scan. (a) OCT intensity image and (b) phase map induced by 800 Hz ARF excitation on the phantom.

amplifier (PAS-000023-25, Spanawave, USA), with a linear gain of 46 dB between 0.15 MHz and 230 MHz. Lateral scans were only made within the ultrasound focal zone, where we assumed that the acoustic radiation force that was used to induce particle displacement was evenly distributed.

The feasibility of the proposed confocal ARF-OCE system was first investigated on silicone phantoms with different stiffnesses, which were controlled by the ratio of silicone to its associated activator. The displacement of the sample over time, which is used to quantify the tissue stiffness,[22] is linearly proportional to the adjacent A-line phase shift at each lateral location and was calculated according to Eq. (2), in the same manner as our previous work. In Eq. (2), d denotes the local displacement, $\Delta\varphi(x,z,t)$ is the measured A-line phase shift for each data point, λ_0 is the centerwave length for OCT light source, n is the tissue refractive index, and τ indicates the CCD integration time for OCT imaging. From the ARF-OCE measurement, the displacements were 0.198 μm for the silicone phantom with a 1:30 ratio of the silicone to the activator and 0.28 μm for the second phantom with a ratio of 1:26, respectively

$$d = \int_{t_1}^{t_2} \frac{\Delta\varphi(x,z,t)\lambda_0}{4\pi n\tau}. \tag{2}$$

The Young's moduli for phantoms with 1:26 and 1:30 ratio of the silicone to the curing agent were 75.1 and 53.7 kPa, respectively, which were measured under a compression test yielding a Young's modulus ratio around 1:1.40, similar to the calculated displacement ratio from our ARF-OCE measurements of 1:1.41. The results indicate that the displacement from our confocal ARF-OCE system is able to provide a reliable relative Young's modulus for the materials.

We further characterized our confocal ARF-OCE system on an agar phantom with a stainless steel sphere (513 μm in diameter) embedded in the center. The phantom was placed about 50 mm below the surface of the US transducer and immersed in water. While the phantom was stimulated at a square wave modulation frequency of 1050 Hz, 3D scans, consisting of 150 frames, were made at 9.8 frames per second with 2048 A-lines per frame, covering a 0.5 mm by 0.3 mm area over the sphere [Fig. 3(c)]. The elastograph was reconstructed afterwards. Due to the penetration limitation

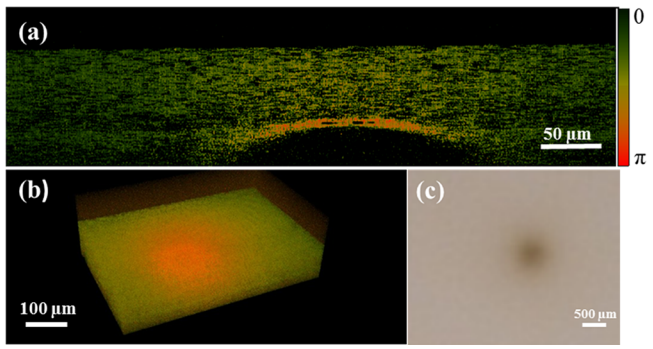

FIG. 3. 2D and 3D ARF-OCE ((a) and (b)) and the sample image of the agar phantom (c) with a stainless steel sphere embedded inside stimulated at a fixed frequency of 1050 Hz.

of OCT imaging, only the top portion of the stainless steel ball is shown in the images. From the 2D elastograph, we observed a substantial difference in the vibration amplitude between the sphere and the agar. As expected, the surface of the sphere and the area above produced distinctive phase vibrations compared with the rest of the phantom, yielding a high contrast area in OCE images [Figures 3(a) and 3(b)]. The results indicate that our confocal ARF-OCE system can efficiently differentiate materials of different stiffnesses.

Finally, we tested our confocal ARF-OCE technique on a section of a human cadaver coronary artery to investigate its potential in intravascular imaging to resolve plaque composition. Atherosclerosis is a complex disease, in which multiple plaques build up within the arteries, altering the mechanical property of the arteries. Visualizing plaques to help understand the progression of disease and to aid in diagnosis and treatment is highly desirable. The artery sample was cut open, flattened, mounted with a fixed bottom [Fig. 4(f)] and immersed in a water tank filled with a phosphate buffered saline solution to maintain the osmolarity of the cells. A 500 Hz-square wave-modulation frequency was applied to stimulate the tissue during the experiment. The sample was scanned three-dimensionally over a 0.5 mm by 0.3 mm area within 15.4 s at the position indicated in Fig. 4(f) by the red dashed box. The 0.24 μm A-line spacing used in the 3D data acquisition has sufficient oversampling for phase calculation. 2D and 3D structural images and elastograms were reconstructed [Figs. 4(a)–4(e)]. The sample was diagnosed as fibroatheroma with a necrotic core (NC) according the histological information [Fig. 4(g)]. In the 3D OCT image, shown in Fig. 4(a), a general morphological view of the tissue was obtained, but no obvious evidence of atherosclerosis was found based on the optical scattering property. However, in Fig. 4(b), a strong vibration phase contrast can clearly be seen in the ARF-OCE image. The NC and fibrous cap (FC) in the plaque, identified in the histological section, may contribute to the vibration phase difference shown in the 3D ARF-OCE image. Fig. 4(c), the fused OCT and OCE image illustrates the fact that ARF-OCE provides additional imaging contrast which can be used to identify different tissue types based on tissue mechanical properties. The detailed correlation between pathology and the OCE map is shown in 2D images. The 2D OCT image [Fig. 4(d)] shows the structure of the artery segment where the distinction between different tissue types is barely discernable.

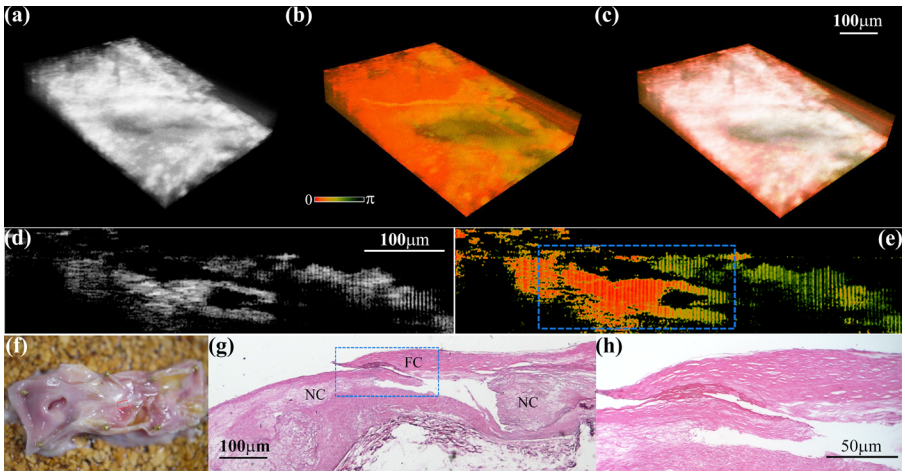

FIG. 4. (a) 3D OCT image, (b) 3D ARF-OCE phase image of a human cadaver coronary artery, (c) fused OCT and ARF-OCE images, (d) 2D OCT, (e) 2D ARF-OCE, (f) sample image, (g) histological image, (h) close-up view of the atherosclerotic lesion. FC: fibrous cap, NC: necrotic core.

However, it is apparent that there is a significant displacement difference between the FC on the top right and the NC on the left from the 2D elastograph [Fig. 4(e)], which shows the elasticity difference between the two tissue types. The dark green area represents larger phase vibrations (softer tissue) and the red color area within the blue dashed box indicates smaller phase vibrations (stiffer tissue). These results demonstrate the ability of our confocal ARF-OCE method to differentiate micro-scaled biomechanical property alterations in human tissues, which is especially significant when the optical scattering properties alone cannot provide substantial evidence to identify the lesions.

In summary, a confocal ARF-OCE system was developed with simultaneous confocal ARF stimulation and OCE detection. Featuring high axial resolution, high speed, and high motion sensitivity, the confocal setup also promises great potential for point by point elastic imaging *in vivo*. Quantitative displacement measurements were made on phantoms, demonstrating the ability of our method for mapping the relative elastic property of materials. Both phantom and human tissue tests indicate that this method is able to differentiate materials with distinctive stiffnesses. Our confocal ARF-OCE technique is compatible with intravascular probes and holds great promise for *in vivo* differentiation of tissues of different types and may also offer the potential to identify the composition in atherosclerotic lesions which is of great importance for atherosclerosis diagnosis and treatment.

This work was supported by the National Institutes of Health (R01EB-10090, R01EY-021529, R01-HL-105215, R01-HL103764, and P41EB-015890), Air Force Office of Scientific Research (FA9550-04-0101), and the Arnold and Mabel Beckman Foundation. Dr. Chen has a financial interest in OCT Medical, Inc., which, however, did not support this work.

[1]G. C. Cheng, H. M. Loree, R. D. Kamm, M. C. Fishbein, and R. T. Lee, Circulation **87**(4), 1179–1187 (1993).
[2]J. Ophir, I. Céspedes, H. Ponnekanti, Y. Yazdi, and X. Li, Ultrasonic Imaging **13**(2), 111–134 (1991).
[3]C. L. de Korte and A. F. W. van der Steen, Ultrasonics **40**(1-8), 859–865 (2002).
[4]C. L. de Korte, A. F. W. van der Steen, E. I. Cespedes, G. Pasterkamp, S. G. Carlier, F. Mastik, A. H. Schoneveld, P. W. Serruys, and N. Bom, Phys. Med. Biol. **45**(6), 1465–1475 (2000).
[5]J. A. Talwalkar, D. M. Kurtz, S. J. Schoenleber, C. P. West, and V. M. Montori, Clin. Gastroenterol. Hepatol. **5**(10), 1214–1220 (2007).
[6]D. B. Plewes, J. Bishop, A. Samani, and J. Sciarretta, Phys. Med. Biol. **45**(6), 1591–1610 (2000).
[7]D. A. Woodrum, A. J. Romano, A. Lerman, U. H. Pandya, D. Brosh, P. J. Rossman, L. O. Lerman, and R. L. Ehman, Magn. Reson. Med. **56**(3), 593–600 (2006).
[8]M. Yin, J. A. Talwalkar, K. J. Glaser, A. Manduca, R. C. Grimm, P. J. Rossman, J. L. Fidler, and R. L. Ehman, Clin. Gastroenterol. Hepatol. **5**(10), 1207–1213 (2007).
[9]A. S. Khalil, R. C. Chan, A. H. Chau, B. E. Bouma, and M. R. K. Mofrad, Ann. Biomed. Eng. **33**(11), 1631–1639 (2005).
[10]H. J. Ko, W. Tan, R. Stack, and S. A. Boppart, Tissue Eng. **12**(1), 63–73 (2006).
[11]R. K. Wang, Z. Ma, and S. J. Kirkpatrick, Appl. Phys. Lett. **89**(14), 144103 (2006).
[12]B. F. Kennedy, T. R. Hillman, R. A. McLaughlin, B. C. Quirk, and D. D. Sampson, Opt. Express **17**(24), 21762–21772 (2009).
[13]J. Rogowska, N. A. Patel, J. G. Fujimoto, and M. E. Brezinski, Heart **90**(5), 556–562 (2004).
[14]B. F. Kennedy, X. Liang, S. G. Adie, D. K. Gerstmann, B. C. Quirk, S. A. Boppart, and D. D. Sampson, Opt. Express **19**(7), 6623–6634 (2011).
[15]M. Razani, A. Mariampillai, C. Sun, T. W. H. Luk, V. X. D. Yang, and M. C. Kolios, Biomed. Opt. Express **3**(5), 972–980 (2012).
[16]W. Qi, R. Chen, L. Chou, G. Liu, J. Zhang, Q. Zhou, and Z. Chen, J. Biomed. Opt. **17**(11), 110505 (2012).
[17]C. Li, G. Guan, X. Cheng, Z. Huang, and R. K. Wang, Opt. Lett. **37**(4), 722–724 (2012).
[18]S. G. Adie, X. Liang, B. F. Kennedy, R. John, D. D. Sampson, and S. A. Boppart, Opt. Express **18**(25), 25519–25534 (2010).
[19]R. K. Manapuram, S. R. Aglyamov, F. M. Monediado, M. Mashiatulla, J. Li, S. Y. Emelianov, and K. V. Larin, J. Biomed. Opt. **17**(10), 100501 (2012).
[20]Y. Sun, A. J. Chaudhari, M. Lam, H. Xie, D. R. Yankelevich, J. Phipps, J. Liu, M. C. Fishbein, J. M. Cannata, K. K. Shung, and L. Marcu, Biomed. Opt. Express **2**(8), 2288–2298 (2011).
[21]Y. Sun, J. Park, D. N. Stephens, J. A. Jo, L. Sun, J. M. Cannata, R. M. G. Saroufeem, K. K. Shung, and L. Marcu, Rev. Sci. Instrum. **80**(6), 065104 (2009).
[22]E. Chen, R. Adler, P. Carson, and W. Jenkins, Ultrasound Med. Biol. **21**(9), 1153–1162 (1995).